Check for updates

ADVANCED MATERIALS
www.advmat.de

Directionally Modulated Zinc Deposition by a Robust Zincophilic Cu-Phthalocyanine Protective Layer in Dendrite-Free Aqueous Zinc Ion Batteries

Yidi Wang, Xinwei Jiang, Wenhao Liang, Benjamin Tawiah, Yang Wang, Hao Jia,* and Wai-Yeung Wong**

The directional modulation of zinc (Zn) deposition with further investigation of the dendrite-formation mechanism is vital in artificial anode protective layer for aqueous Zn-ion batteries (AZIBs). Herein, a robust metalated covalent organic framework (CuPc-COF) used as the artificial anode protective layer is proposed, in which the zincophilic sites of π-conjugated periodic skeletons are precisely designed to modulate the directional migration of Zn^{2+}, the multiple redox-active sites facilitate the Zn^{2+} confinement and transfer, and the central metal copper (Cu) serves as the inhibitor to eliminate the hydrogen evolution side reactions. By combining theoretical calculations with experiments, the π-conjugated planar CuPc-COF layer is a desired protective coating of AZIB anodes with directionally transport channels and abundant redox active sites, thus inducing two-dimensional deposition of Zn. Attributed to these superiorities, the fabricated CuPc-COF@Zn anode demonstrates excellent cycling lifespan in both symmetrical cell (exceeding 2500 h at 1 mA cm^{-2}) and full cell with different cathodes (more than 3000 cycles at 1 A g^{-1}), outperforming most reported zinc anodes with COF-based layers.

1. Introduction

Energy storage technologies have advanced significantly due to the growing demand for energy storage devices with high energy densities. As a result, alternative energy storage systems (ESS) besides lithium-ion batteries have piqued research interest.[1] Among these, aqueous zinc ion batteries (AZIBs) have received significant attention lately due to their potential applications in large-scale energy storage and portable electronics resulting from their low cost, high safety rating, eco-friendliness, and high power density.[2] Despite these novel properties, their practical applications are currently hindered as a result of the inferior zinc (Zn) anode performance due to the uncontrollable Zn dendrite growth evoked by the inhomogeneous Zn nucleation and the unwanted hydrogen evolution in the aqueous electrolytes. These reactions induce continuous corrosion, internal short circuit, and rapid capacity fading accompanied by the consumption of both electrolyte and active Zn metal, making the pursuit of durable AZIB anode a formidable challenge.[3] There have been significant efforts in the past few years to engineer zinc anode devoid of dendrite formation and its accompanying side effects.[4] Artificial interfacial engineering is a straightforward and effective approach for preventing zinc dendrite formation and its negative effects.[5] A variety of materials including organic polymers,[6] carbon-based materials,[7] metal oxides,[8] metal–organic frameworks (MOFs),[9] and covalent organic frameworks (COFs)[10] have been reported as effective protecting materials for Zn anodes.

Recently, COFs, as an emerging class of crystalline and porous polymeric material, assembled from light components (C, N, O, etc.) through strong covalent bonds, are regarded as the potential candidate for building artificial protective layers of Zn anodes. COF-based Zn anode protecting layer with a tunable skeleton, highly ordered and porous structure, and abundant redox-active groups, allows rapid and exclusive transport of carriers and accelerates the ion transmission kinetics during repeated cycles.[10] For example, Mi's group designed a functional vinylene-linked COF-based interface layer with abundant zincophilic fluorinated

Y. Wang, W. Liang, Y. Wang, W.-Y. Wong
Department of Applied Biology and Chemical Technology and Research Institute for Smart Energy
The Hong Kong Polytechnic University
Hung Hom, Hong Kong 999077, P. R. China
E-mail: yang1.wang@polyu.edu.hk; wai-yeung.wong@polyu.edu.hk

X. Jiang, H. Jia
Key Laboratory of Eco-Textiles
Ministry of Education
Jiangnan University
Wuxi, Jiangsu 214000, P. R. China
E-mail: jiahao@jiangnan.edu.cn

B. Tawiah
Department of Industrial Art
Kwame Nkrumah University of Science and Technology
PMB, Kumasi Kumasi AK-039-5028, Ghana

The ORCID identification number(s) for the author(s) of this article can be found under https://doi.org/10.1002/adma.202503086

© 2025 The Author(s). Advanced Materials published by Wiley-VCH GmbH. This is an open access article under the terms of the Creative Commons Attribution-NonCommercial-NoDerivs License, which permits use and distribution in any medium, provided the original work is properly cited, the use is non-commercial and no modifications or adaptations are made.

DOI: 10.1002/adma.202503086

sites that manipulate the Zn plating/stripping behaviors and suppress interfacial side reactions simultaneously.[10a] Benefiting from the tunable structures of COF materials, Zheng's group proposed a series of COFs with different Zn^{2+} transport channels to accelerate the ion transfer kinetics, at the same time, facilitating rapid diffusion and regulation of homogeneous Zn^{2+} flux.[10b] Nonetheless, almost all the reported COF layers focus on the successful construction of well-ordered channels, thereby ignoring the delicate design of the COF functional structures, like introducing more zincophilic sites or inert metal ions.[10a–f] Thus, the inherent shortcomings, such as low Zn^{2+} affinity, side reactions, and serious volume changes during cycling, have not been ameliorated, and still affect the cycling stability of Zn anodes to some extent.[10g] Placing transition metal centers into the COF building blocks offers a convenient way to significantly tune their structural diversity, modify their electronic properties, and achieve advanced functional materials.[11] Such highly conjugated organometallic COF materials with multi-electron redox chemistry will potentially offer a good avenue toward the Zn^{2+} transmission kinetics due to their easily adjustable structure and reversible redox processes that are favorable to the generation of electrical bistate or multistate. On the other hand, the introduction of inert metal, like copper (Cu), owing to the strong zincophilicity and inactive nature for hydrogen evolution reaction (HER),[12] effectively improves Zn^{2+} transmission kinetics and alleviates hydrogen evolution and anode corrosion in aqueous electrolytes. It has, therefore, become crucial to rationally engineer a metallated COF protective layer, not only providing ample uniform Zn^{2+} transport channels, abundant redox-active sites, and ultrahigh Zn^{2+} affinity, but also presenting the excellent inherent adhesion, inhibited hydrogen evolution and protective functionality, to promote the de-solvation of hydrated Zn^{2+}, accelerate the ion transfer kinetics, regulate the Zn-ion flux, and realize dendrite-free AZIBs.

In this context, a robust COF as a reliable anode protective layer was delicately designed, in which the 18 electrons π-conjugated planar compound copper-phthalocyanine (Cu-Pc) serves as the main building block, the metal-N_4 coordination centers, dioxin linkers, and ketone groups in the periodic skeletons are regarded as reversible electrochemical redox couples,[13] and the central metal Cu possessing strong zincophilicity and inert nature for HER, is expected to effectively inhibit the hydrogen evolution and anode corrosion. Moreover, the highly conjugated periodic skeletons with rich redox-active sites showed only a small volumetric deformation after zincation, as confirmed by the experimental and theoretical studies, thereby maintaining stable chemical properties and structure during the long-time cycles. With the CuPc-COF as the anode protective layer, COF@Zn symmetrical cells exhibited an outstanding reversible capacity (over 99% average Coulombic efficiency), high-rate capability (5 mA•cm^{-2}), and superior long-time cycling performance for 2500 h (1 mA•cm^{-2}); The full cell application with $NH_4V_4O_{10}$ (NHVO) or I_2 cathodes both delivered good cyclability (89.1% retention ratio after 1000 cycles or 92.9% retention ratio after 3000 cycles), outperforming the most previously reported AZIBs with COF-based layers and illustrating its potential for practical application in Zn-based electrochemical energy storage and conversion devices.

2. Results and Discussion

The designed dioxin-linked CuPc-COF was synthesized by the coupling reaction between octahydroxy metal-phthalocyanine ($CuPc(OH)_8$) and tetrafluoroanthraquinone (TFAQ) in the presence of potassium carbonate (K_2CO_3) and dimethylacetamide (**Figure 1**a). This was made possible by the multiple redox-active sites for the confinement and transfer of Zn^{2+}, including the dioxin, and ketone groups in sp^2-carbon conjugated periodic phthalocyanine frameworks (18 delocalized π electrons). To evaluate the possibility and feasibility of Zn^{2+} migration in this COF, density functional theory (DFT) calculations were performed to simulate the CuPc-COF structures and the Zn plating/stripping processes.

Based on the electronegativity analysis of CuPc-COF structure (Figure 1b top), four zincophilic sites were predicted to accommodate Zn^{2+} inside the pores to form a highly symmetric CuPc-COF-Zn geometry (Figure 1b bottom). The Zn^{2+} ions were located at the center of the COF pore (site 1); close to the Cu atom (site 2); adjacent to N (site 3), and O (site 4) atoms labeled in Figure 1c. Accordingly, the adsorption energies of one Zn^{2+} binded to the different sites of the CuPc-COF periodic unit and bare Zn plate were calculated by DFT and compared in Figure 1c. The optimized adsorption structures of Zn^{2+} with bare Zn are shown in Figure S1 (Supporting Information). Among them, Zn^{2+} located at sites 3 and 4, possessed the binding energies of −2.15 and −2.28 eV, respectively, which were much lower than that of Zn^{2+} located at sites 1, 2, and bare Zn. Thus, the Zn^{2+} preferred to be clamped by the electronegative N and O atoms, which corresponded to the simulated zincophilic sites of CuPc-COF pores in electrostatic potential (ESP) analysis based on one repeat unit. As illustrated in Figure 1b top, the ESP result showed that the negative charge maxima (red area) were surrounded by highly electronegative O and N atoms and distributed inside the tetragonal pore of the CuPc-COF unit, implying suitable Zn^{2+} accommodation sites. Meanwhile, the ESP result (Figure 1b bottom) of CuPc-COF after zincification revealed that the most negatively charged areas were trapped by all the Zn^{2+}.

The crystalline structures of the products were analyzed by powder X-ray diffraction (PXRD) in combination with theoretical structural simulations (Figure 1d–f). The major peaks at 3.5°, 7.1°, 11.0°, and 25.7° agreed well with the (100), (200), (300), and (001) crystal planes of CuPc-COF, respectively. Based on the Bragg's law, the peak at 3.5° indicated a long-range ordered structure of the ab-plane with a centre-to-centre distance of 25.1 Å, and the broad peak at 25.7° is consistent with an average interlayer distance of 3.6 Å. The periodic DFT calculations on a two-layer $1 \times 1 \times 2$ supercells were performed to obtain the stable structures and lattice information of AA and AB stacking models. The free energy data and XRD diffraction patterns were also simulated based on the optimized structures. First, the fully eclipsed AA-stacking model (Figure 1e) showed lattice parameters $\alpha = \beta = \gamma = 90°$, a = b = 25.1 Å, and c = 3.5 Å, and alternative staggered AB-stacking model (Figure 1f) with offset distances showed lattice parameters $\alpha = \beta = \gamma = 90°$, a = b = 25.1 Å, and c = 3.3 Å. By comparing the simulated PXRD patterns of the optimized structures with the experimental patterns, the Pawley refinement was carried out with the results R_{wp} = 2.84% and R_p = 2.14% (Figure 1d, green curve), which is well consistent with

© 2025 The Author(s). Advanced Materials published by Wiley-VCH GmbH

15214095, 2025, 33, Downloaded from https://advanced.onlinelibrary.wiley.com/doi/10.1002/adma.202503086 by HONG KONG POLYTECHNIC UNIVERSITY HU NG HOM, Wiley Online Library on [28/09/2025]. See the Terms and Conditions (https://onlinelibrary.wiley.com/terms-and-conditions) on Wiley Online Library for rules of use; OA articles are governed by the applicable Creative Commons License

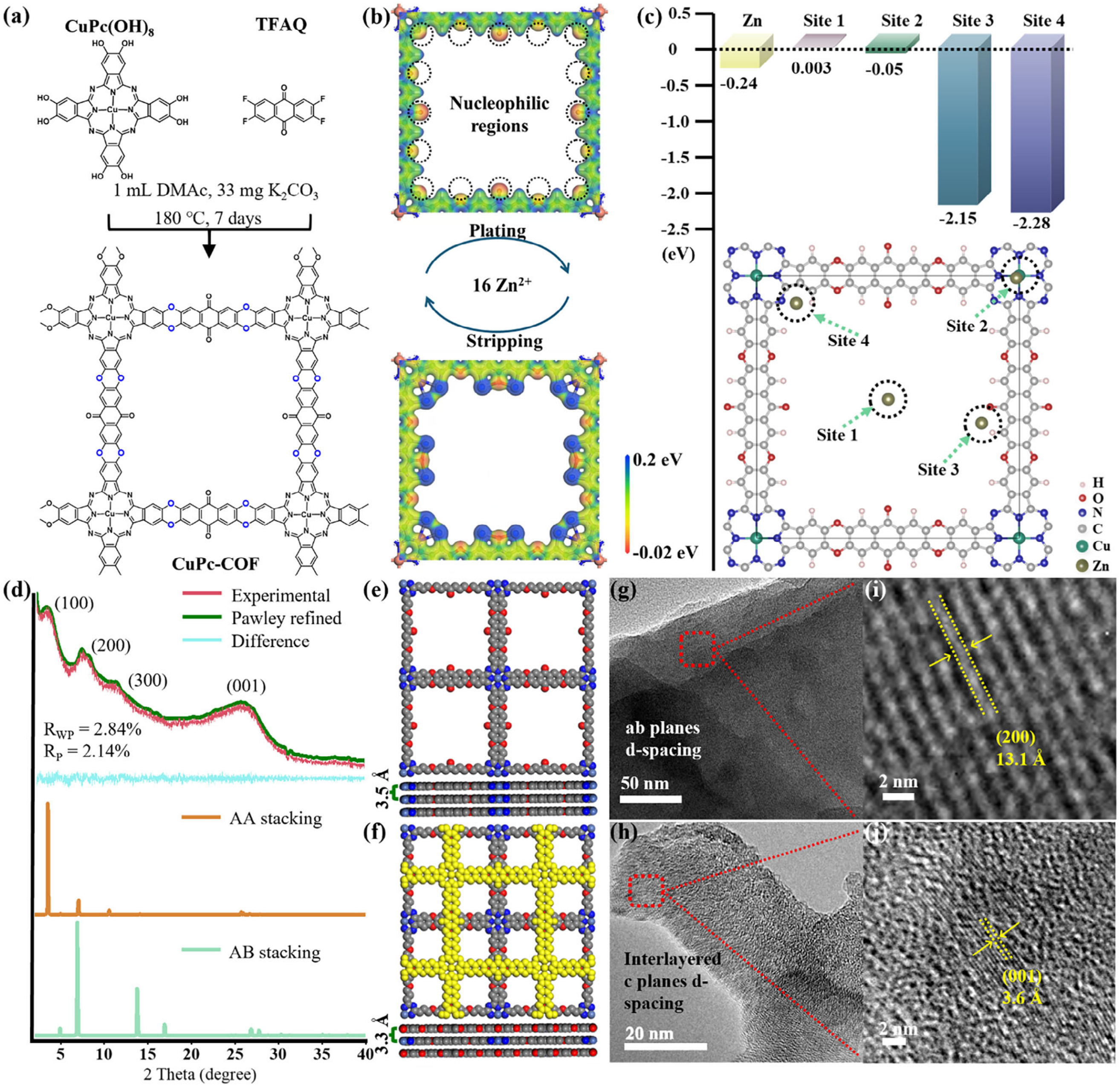

Figure 1. a) Schematic illustration of the reaction between CuPc(OH)$_8$ and TFAQ to form CuPc-COF. Theoretical simulation and schematic illustration for Zn^{2+} storage in CuPc-COF: b) Mapped electrostatic potential (ESP) diagram of the CuPc-COF and 16Zn-CuPc-COF repetitive units on the van der Waals surface. The dotted circles represent possible active sites. c) The proposed adsorption energies of Zn^{2+} located on the different sites of CuPc-COF. Structural characterization of CuPc-COF with dioxin linkages: d) PXRD patterns of CuPc-COF (Experimental result; Pawley refined pattern; Difference; AA stacking and AB stacking); e) top (top) and side (bottom) views of the AA stacking model; f) top (top) and side (bottom) views of the AB stacking model; g,h) TEM images and i,j) magnified lattice fringes of CuPc-COF.

the simulated PXRD pattern of AA stacking (Figure 1d, orange curve). Based on the above results, the thermodynamically stable conformation of CuPc-COF proved to be an AA stacking geometry with square cells (a = b = 25.1 Å, c = 3.5 Å). This bulk COF product presented stacked microscale sheets as illustrated by the scanning electron microscopy (SEM) images (Figure S2, Supporting Information). The high-resolution transmission electron microscopy (HRTEM) showed the distinct lattice fringes of the CuPc-COF. The clear lattice spacings of 13.1 and 3.6 Å in Figure 1i,j were identified to be the crystal planes (200) and (001), respectively, which was well consistent with the simulated structure in Figure 1e. The surface areas and porosity of CuPc-COF were analyzed by N$_2$ adsorption/desorption measurements at 77.3 K (Figure S3, Supporting Information). The Brunauer–Emmett–Teller (BET) surface area of CuPc-COF was 163 m^2•g^{-1}. The pore size distribution revealed that the CuPc-COF possessed

15214095, 2025, 33, Downloaded from https://advanced.onlinelibrary.wiley.com/doi/10.1002/adma.202503086 by HONG KONG POLYTECHNIC UNIVERSITY HU NG HOM, Wiley Online Library on [28/09/2025]. See the Terms and Conditions (https://onlinelibrary.wiley.com/terms-and-conditions) on Wiley Online Library for rules of use; OA articles are governed by the applicable Creative Commons License

© 2025 The Author(s). Advanced Materials published by Wiley-VCH GmbH

micropores centered at ≈3.60 nm, consistent with the simulated pore diameter shown in Figure 1e.

A variety of structural characterizations, including solid-state ^{13}C nuclear magnetic resonance (ssNMR) spectroscopy, Fourier transform infrared spectroscopy (FT-IR), and X-ray photoelectron spectroscopy (XPS) were performed to explore the chemical structure of CuPc-COF. As illustrated in Figure S4 (Supporting Information), the resonance signals in the ^{13}C NMR spectrum at ≈180, 145, 127, and 110 ppm can be assigned to C—N, C═O groups, carbons on the Pc and phenyl groups, respectively. Additionally, the FT-IR spectrum (Figure S5, Supporting Information) of CuPc-COF showed vibrational bands at ≈1050 and ≈1300 cm^{-1}, corresponding to the characteristic asymmetric and symmetric stretching modes of dioxin C–O, respectively. Moreover, the overall XPS survey spectrum indicates that the CuPc-COF contains C, O, N, and Cu, elements (Figure S6, Supporting Information). The higher solution spectrum (Figure S7, Supporting Information) of C 1s evidenced the key groups of C═O, C—O, C—N, and C═C. The two peaks of the O 1s spectrum can be attributed to the C—O—C bond of dioxin linkages, and the C═O bond of quinone. These results are consistent with the results of the FTIR analysis, further confirming that the dioxin-linked CuPc-COF was successfully synthesized.

Based on the aforementioned results, the synthesized CuPc-COF served as an artificial protection coating to stabilize the Zn anode. The CuPc-COF@Zn (denoted as COF@Zn) anodes were fabricated by doctor casting onto the Zn surface based on CuPc-COF powder and polyvinylidene fluoride (PVDF) suspension (see Supporting Information for details). By comparing the morphology and surface properties from SEM images (**Figure 2**a,b), the COF@Zn electrode depicts a homogeneous and porous surface with abundant cavities, while the bare Zn anode exhibits a rough surface full of gills. Besides, the SEM cross-sectional view of the COF@Zn electrode presents a dense coating with a thickness of ≈10 µm (Figure 2c). Afterward, the bare Zn and COF@Zn anodes were investigated at a high current density of 10 mA cm^{-2} and a capacity of 10 mAh cm^{-2} and their surface morphology evolution during the constant current plating/stripping cycles was monitored using optical microscopy. As shown in Figure 2d, the bare Zn electrode displayed a smooth edge before cycling. After 30 min, the scattered dark Zn nucleus was clearly observed on the bare Zn surface, and protrusions grew along the edge of the bare Zn electrode with the extended plating time and finally became "dead Zn", which evidences uneven Zn plating. In contrast, there is still no sign of protrusions or Zn dendrite generation of the COF@Zn electrode, which remains a uniform and compact surface benefiting from the protection of the COF layer.

Moreover, the linear sweep voltammetry (LSV) measurement was conducted to compare the hydrogen evolution potentials of different electrodes in the aqueous electrolyte (2 м $ZnSO_4$). As shown in Figure 2f, the hydrogen evolution potential of COF@Zn (−1.14 V) was lower than that of the bare Zn (−1.11 V), indicating an effective HER suppression function of the CuPc-COF layer. The Coulombic efficiency (CE) of different anodes was then investigated in asymmetric Zn/Ti cells at 1 mA•cm^{-2} (Figure 2g). For bare Zn/Ti cells, a low CE at the initial cycles' contours originated from a lattice fitting stage during the plating/stripping of Zn on Ti substrate and became stable at ≈96%. After 50 cycles, the CE started to fluctuate tempestuously due to the undesirable side reactions caused by inhomogeneous Zn^{2+} flux and short-circuiting.[14] In contrast, the COF@Zn/Ti cells reached an average CE of 99% and retained over 200 cycles, evidencing the successful modulation of Zn deposits and the enhanced Zn affinity of the COF@Zn anode as confirmed by the lower nucleation overpotential (39 mV) of the COF@Zn electrode than that (57 mV) of the bare Zn electrode (Figure 2h). In addition, the COF@Zn electrodes were further assembled to evaluate the cyclic performance of symmetrical cells using galvanostatic charge/discharge procedures (Figure 2i). As a contrast, the Zn symmetrical cells showed a fluctuating overpotential and encountered an abrupt collapse after 220 h at 1 mAh•cm^{-2} due to the dendrite-induced short circuit. Benefiting from the engineered CuPc-COF layer, the COF@Zn symmetrical cells maintained a superior cycling property for 2500 h. Besides, the inhibited voltage hysteresis of COF@Zn symmetrical cells can be ascribed to the effective function of COF layer on reducing the local current density.[15] More impressively, COF@Zn symmetrical cells also exhibited an enhanced lifespan of more than 250 h at the large current density of 5 mA•cm^{-2} (2.5 mAh•cm^{-2}) as shown in Figure 2j. Impressively, the distinguished electrochemical reversibility of COF@Zn anode surpasses the most recently reported results of AZIBs based on COF-based anode protective layers (Figure S8, Supporting Information). The comparative results indicate that the introduction of COF layer could alleviate interface concentration distribution, reduce Zn deposition barrier, homogenize Zn plating/stripping, and inhibit the dendrite growth, thus realizing a highly reversible Zn plating/stripping procedures and remarkably enhanced ion transmission kinetics.

To further investigate the influence of the CuPc-COF layer on the Zn plating/stripping behavior, the surface morphologies of bare Zn and COF@Zn anodes were analyzed with SEM observation after 200 cycles. As shown in **Figure 3**a,b, numerous irregular flakes on the bare Zn electrode were observed, which can be ascribed to the uneven Zn deposition and severe side reactions.[3b] In contrast, the COF@Zn anode surface was relatively close to its original surface morphology (Figure 2b), and no vertical Zn deposits or dendrites were observed, indicating the excellent stability and uniform Zn deposition during the 200 cycles. Furthermore, the XRD of bare Zn and COF@Zn electrodes after cycling was presented in Figure 3c. As expected, it can be found that the obvious by-product peak of $Zn_4SO_4(OH)_6$•$4H_2O$ occurred in the cycled Zn anode, implying that the CuPc-COF layer could effectively inhibit the by-product formation.[16] Meanwhile, the intensity of the Zn (002) plane peak for the COF@Zn electrode significantly increased after cycling. This indicates that the CuPc-COF layer guided Zn deposition along the (002) orientation, which is key to achieving flat Zn deposition. Additionally, the roughness of the different anodes was compared by using 3D super-depth-of-field microscopy (Figure S9, Supporting Information). The COF interlayer significantly improved the surface flatness of the Zn anode, which demonstrates the significant effectiveness of the COF interlayer in suppressing dendrite growth and side reactions again.

Accordingly, the desolvation process of $Zn(H_2O)_6{}^{2+}$ in the different electrode/electrolyte interfaces was studied, as it is commonly regarded as the rate-limiting procedure of Zn deposition due to the strong interaction of Zn^{2+} and the solvent shell.[17] The activation energy (E_a) was then calculated to evaluate the

© 2025 The Author(s). Advanced Materials published by Wiley-VCH GmbH

15214095, 2025, 33, Downloaded from https://advanced.onlinelibrary.wiley.com/doi/10.1002/adma.202503086 by HONG KONG POLYTECHNIC UNIVERSITY HU NG HOM, Wiley Online Library on [28/09/2025]. See the Terms and Conditions (https://onlinelibrary.wiley.com/terms-and-conditions) on Wiley Online Library for rules of use; OA articles are governed by the applicable Creative Commons License

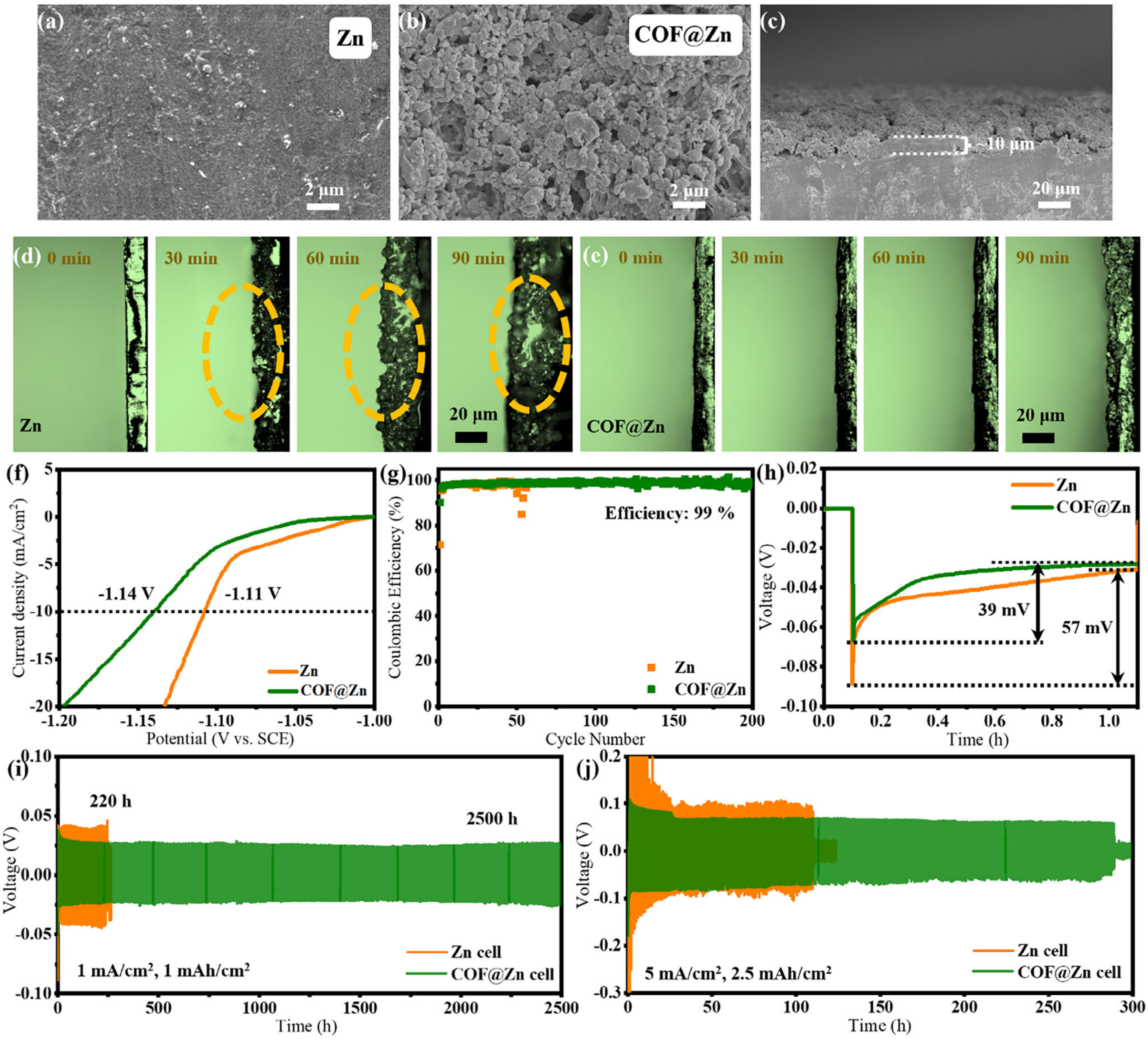

Figure 2. SEM images of the top view of the a) Zn and b) COF@Zn electrodes; c) cross-sectional view of the COF@Zn electrode. In situ optical visualization observations of Zn plating process on d) bare Zn and e) COF@Zn anodes. f) LSV profiles of Zn and COF@Zn electrodes. g) Coulombic efficiencies of Zn plating/stripping in Zn/Ti and COF@Zn/Ti cells. h) Nucleation overpotential of Zn and COF@Zn electrodes at 1 mA cm^{-2}. Comparison of the cycling stability of different symmetry cells at i) 1 mA•cm^{-2} (1 mAh•cm^{-2}) and j) 5 mA•cm^{-2} (2.5 mAh•cm^{-2}).

desolvation capacity of the electrode according to the Arrhenius equation:

$$1/R_{ct} = A\exp\left(-E_a/RT\right) \tag{1}$$

where R_{ct} is the interfacial resistance, A is the frequency factor, R and T present the gas constant and absolute temperature, respectively. As expected, the COF interphase remarkably reduced the E_a of the Zn anode from 50.05 to 41.82 kJ mol^{-1} (Figure S10, Supporting Information; Figure 3d). It demonstrated that $Zn(H_2O)_6^{2+}$ tends to bond with the redox groups of COF and greatly facilitates the desolvation process, profiting from the rationally designed layer.[18]

To understand the influence of the CuPc-COF layer on the regulation of the Zn deposition environment, the electric field and Zn^{2+} concentration distributions of bare Zn and COF@Zn electrodes were simulated via the finite element model. Based on the results in Figure 3e, there is an uneven localized electric field over the surface of the bare Zn electrode, along with local charge and Zn^{2+} aggregation. This relates to the inevitable "tip effect" of pure Zn, which leads to local Zn nucleation and deposition, ultimately resulting in the formation of Zn dendrites. By comparison, COF@Zn yields a more compact electric field distribution in a longer-range order along the whole anode surface, which effectively optimizes the microenvironment at the Zn/electrolyte interface and inhibits the localized Zn^{2+} concentration

© 2025 The Author(s). Advanced Materials published by Wiley-VCH GmbH

15214095, 2025, 33, Downloaded from https://advanced.onlinelibrary.wiley.com/doi/10.1002/adma.202503086 by HONG KONG POLYTECHNIC UNIVERSITY HU NG HOM, Wiley Online Library on [28/09/2025]. See the Terms and Conditions (https://onlinelibrary.wiley.com/terms-and-conditions) on Wiley Online Library for rules of use; OA articles are governed by the applicable Creative Commons License

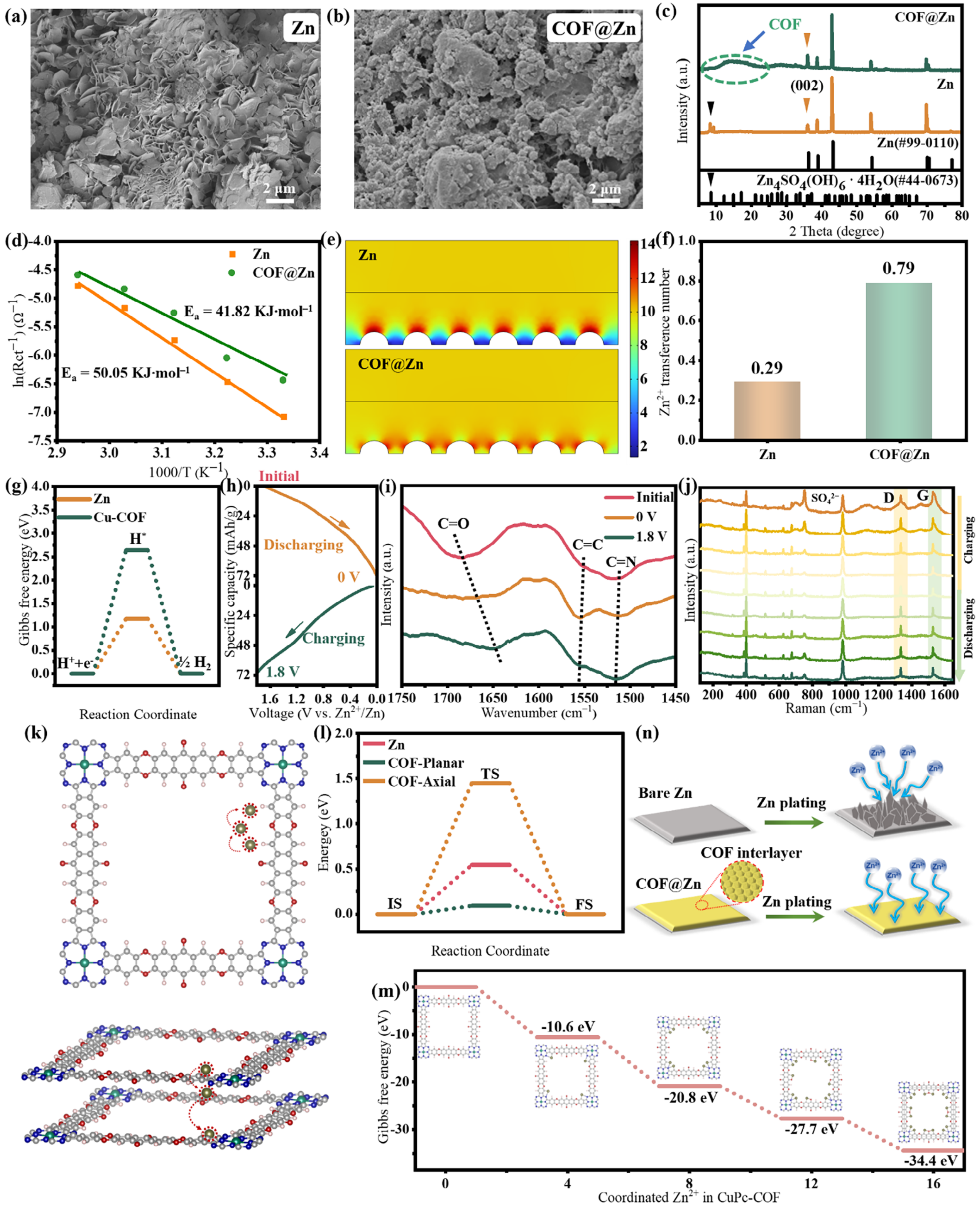

15214095, 2025, 33, Downloaded from https://advanced.onlinelibrary.wiley.com/doi/10.1002/adma.202503086 by HONG KONG POLYTECHNIC UNIVERSITY HU NG HOM, Wiley Online Library on [28/09/2025]. See the Terms and Conditions (https://onlinelibrary.wiley.com/terms-and-conditions) on Wiley Online Library for rules of use; OA articles are governed by the applicable Creative Commons License

© 2025 The Author(s). Advanced Materials published by Wiley-VCH GmbH

polarization for dendrite growth. Meanwhile, the Zn^{2+} transference number ($t_{Zn}{}^{2+}$) was measured under a constant 10 mV polarization potential using Electrochemical Impedance Spectroscopy (EIS) and voltage-time curves (Figure S11, Supporting Information). Notably, the $t_{Zn}{}^{2+}$ of the COF@Zn anode increased significantly from 0.29 to 0.79 compared to the bare Zn anode (Figure 3f). It reveals that the COF@Zn structure with uniform transfer channels could accelerate the decoupling of Zn^{2+}, provide sufficient Zn^{2+} for subsequent diffusion and nucleation, and induce a low-resistance pathway.

Considering the improved interfacial Zn deposition on CuPc-COF and suppressed side reactions, the anti-corrosion property of COF@Zn anode was investigated. As depicted in Figure 2f, the lower HER overpotential of COF@Zn (−1.14 V) indicates the HER inhibition property of CuPc-COF. Meanwhile, the Tafel plots in Figure S12 (Supporting Information) showed that the corrosion potential of COF@Zn slightly shifted toward the positive side, representing a good anticorrosion property of the CuPc-COF coating. In addition, the wettability of the electrode surfaces is an important factor that strongly affects the corrosion and HER behavior. As shown in Figure S13 (Supporting Information), the COF@Zn electrode exhibited an enhanced hydrophobicity with a contact angle of 129.2° in comparison to that of the bare Zn surface (97.5°), indicating the ability of the hydrophobic COF layer to hinder free-water access to the inner Helmholtz plane of the electrode, thus restricting the decomposition of water and the subsequent corrosion and HER processes.[19] To deeply explore the mechanism of CuPc-COF in the Zn plating process, density functional theory (DFT) calculations were performed to determine the Gibbs free energy of the HER for CuPc-COF and bare Zn (Figure 3g). The calculated free energy of hydrogen adsorption (ΔG_{H*}) value of CuPc-COF is 2.65 eV, which is higher than that for the bare Zn (1.15 eV), further corroborating the suppressed HER for CuPc-COF, in line with the aforementioned findings. From the above analysis, it can be concluded that the CuPc-COF protective layer can greatly inhibit the side reactions (corrosion and H_2 evolution) at the anode/electrolyte interface.

To gain a deeper insight into the mechanism for the stabilization and limitation of Zn^{2+} flux by CuPc-COF layer, the state-of-zincification-dependent samples were analyzed by ex situ FT-IR, in situ Raman, and XPS techniques to investigate the migration-controlled Zn^{2+} behaviors during the zincification/dezincification processes. As shown in Figure 3h,i, when discharged to 0 V for zincification, the observed peak for C═O (≈1673 cm^{-1}) became attenuated and broadened with an identifiable shift, and the signal for C═N (≈1518 cm^{-1}) decreased, suggesting the coordination of C═O and C═N with Zn^{2+} during zincification. The signals of C═O and C═N groups became strong again when charged to 1.8 V revealing the successful dezincification and both C═O and C═N groups in the skeleton were reversible for Zn^{2+} storage. On the other hand, the zincification process caused the deviation of O and N atoms from the conjugated COF skeleton, resulting in the intensity enhancement of C═C groups, thereby the signals of C═C groups (≈1560 cm^{-1}) performed conversely with that of the C═O and C═N groups. Furthermore, this FT-IR analysis exhibited the controlled chemical functionalization of multiple redox-active sites in the CuPc-COF for Zn^{2+} storage, matching well with the theoretical results. In addition, in situ Raman spectro-electrochemistry was performed to monitor the chemical structure variation of CuPc-COF during the simulated Zn plating and stripping processes, and the results are shown in Figure 3j. First, the Raman spectrum of CuPc-COF is featured by two major bands of D (1333 cm^{-1}) and G (1529 cm^{-1}). The periodic evolution of D and G bands illustrates the change of the molecular vibration during the (de-)insertion of Zn^{2+}.[20] The value of I_D/I_G is calculated and summarized in Figure S14 (Supporting Information), in which I_D/I_G increased during the Zn^{2+} intercalation process and recovered during the deintercalation process. The recovery of the value I_D/I_G after one cycle indicates the structural stability of the COF and the reversible interaction between CuPc-COF and Zn^{2+} during the electrochemical process.[21] In addition, a stable peak at 977 cm^{-1} maintained during the charging/discharging process should be ascribed to the adsorption of $SO_4{}^{2-}$,[20a] which is confirmed by comparing the initial CuPc-COF with that immersed in 2 M $ZnSO_4$ electrolyte. In Figure S15 (Supporting Information), a new peak at 977 cm^{-1} appeared when CuPc-COF was in contact with the $ZnSO_4$ electrolyte. Moreover, another new peak at 401 cm^{-1} appeared only when CuPc-COF was in the charged state (−0.7 V), but not immersed in $ZnSO_4$ electrolyte, which is assigned to the formation of Zn–O during the simulated Zn plating process.[22] Simultaneously, a disappearing/reappearing weak peak at 1458 cm^{-1} revealed the evolution of the C—O bond, further verifying the Zn^{2+} intercalation and deintercalation process with C–O groups.[21b] Furthermore, XPS analysis was performed on the COF@Zn electrode before and after cycling 200 times (Figure S16, Supporting Information). In the pristine electrode, a low trace of Zn was detected in the Zn 2p XPS spectrum, as the existence of the Zn substrate. After cycling, two characteristic peaks were detected at 1044.6 and 1021.6 eV, corresponding to Zn $2p_{1/2}$ and Zn $2p_{3/2}$, respectively.[23] Significantly, these peaks are attributed to the adsorbed Zn^{2+} on the COF@Zn anode surface,[10b] which implies its robust coordination effect with Zn^{2+} during the discharge/charge cycles. Meanwhile, the attenuated peaks observed in the Cu 2p spectra of COF@Zn after cycling show that the minor Cu element almost disappears from the cycled COF@Zn surface, further confirming its strong zincophilicity.

To fully understand the migration behavior of Zn^{2+} in the COF layer, two probable migration routes for Zn^{2+} transport in the

Figure 3. SEM images of a) Zn and b) COF@Zn electrodes after 200 cycles. c) XRD patterns of cycled Zn and COF@Zn electrodes. d) Arrhenius curves and activation energy comparison of Zn and COF@Zn electrodes. e) Electric field distribution of electrolyte for Zn and COF@Zn electrodes during Zn deposition (unit: mol•cm^{-3}). f) Zn^{2+} transference number of Zn and COF@Zn electrodes. g) DFT calculations to study the ΔG_{H*} of HER for CuPc-COF and bare Zn. h) Charge/discharge profiles of COF@Zn electrode during the Zn plating/stripping process. i) Ex situ FT-IR spectrum analysis of CuPc-COF at different zincification/dezincification states. j) In situ Raman spectra (784 nm excited) of CuPc-COF during the charging/discharging process. k) The possible Zn^{2+} migration pathways (top: planar, bottom: axial) on CuPc-COF. l) The calculated migration energy barriers of Zn^{2+} along the CuPc-COF and bare Zn (IS: initial state; TS: transition state; FS: final state). m) The Gibbs energy change (ΔG) of the zincification process for Zn^{2+} coordinated CuPc-COF. n) Schematic Zn deposition behaviors on Zn and COF@Zn electrodes.

© 2025 The Author(s). Advanced Materials published by Wiley-VCH GmbH

15214095, 2025, 33, Downloaded from https://advanced.onlinelibrary.wiley.com/doi/10.1002/adma.202503086 by HONG KONG POLYTECHNIC UNIVERSITY HU NG HOM, Wiley Online Library on [28/09/2025]. See the Terms and Conditions (https://onlinelibrary.wiley.com/terms-and-conditions) on Wiley Online Library for rules of use; OA articles are governed by the applicable Creative Commons License

CuPc-COF were simulated, and their corresponding migration barriers are shown in Figure 3k,l. The two pathways are expressed as planar and axial routes, respectively. The Zn^{2+} migration in the Zn plate was also studied as a control (Figure S17, Supporting Information). The migration barrier of Zn^{2+} along the planar orientation is 0.09 eV, which is lower than the migration barrier along the axial orientation of 1.45 eV and that of the Zn plate (0.544 eV). By comparing the Zn^{2+} migration energy barriers in Figure 3l, the Zn^{2+} prefers to migrate through the planar direction, which implies that the planar configuration of CuPc-COF is more favorable for enhancing Zn^{2+} planar migration. Especially, the abundant redox sites and uniform pores in the COF skeleton could regulate the localized coordination environment of Zn^{2+}, further accelerating the Zn^{2+} diffusion kinetics with even Zn^{2+} flux. Moreover, the charge density difference distribution of CuPc-COF adsorbed with 16 Zn^{2+} in Figure S18 (Supporting Information) also reveals the unbalanced charge distribution between zincophilic sites and Zn^{2+}, corroborating a liable transfer of electrons from the absorbed Zn^{2+} to the CuPc-COF layer.

Based on the experimental results and theoretical DFT calculations, each unit cell of CuPc-COF can accommodate a maximum of 16 Zn^{2+}, and accordingly, the reversible zincification/dezincification processes are simulated step by step in Figure S19 (Supporting Information), and the corresponding Gibbs free energy of the optimized repetitive Zn-CuPc-COF units is illustrated in Figure 3m. In the simulated plating and stripping processes, the highly symmetric CuPc-COF-Zn geometry could accommodate Zn ions step by step (Figure S19, Supporting Information): first, the four corners of the pores are successively occupied by the eight Zn^{2+} close to N atoms with the distance of 2.75 Å, with the different binding energies of −2.64 and −2.57 eV per Zn^{2+} for steps 1 and 2, respectively. Accordingly, another eight Zn^{2+} can be binded to the O atoms of ketone groups, with the different binding energies of −1.70 and −1.69 eV per Zn^{2+} for steps 3 and 4, respectively. After the plating process, the pore size of simulated CuPc-COF-16 Zn geometry decreased from 11.24 Å to 11.01 Å, indicating that the pore structure and planarity of CuPc-COF are well maintained. It suggests that CuPc-COF has a small volumetric deformation after Zn plating, which would be beneficial for ensuring electrode stability during repeated intercalation/deintercalation of the Zn^{2+} flux. This discharging procedure could be divided into four stages, namely, CuPc-COF+4Zn^{2+}, CuPc-COF+8Zn^{2+}, CuPc-COF+12Zn^{2+}, and CuPc-COF+16Zn^{2+} (Figure 3m). Specifically, the Gibbs energy change of CuPc-COF gradually decreased along with the increased Zn^{2+} coordinated in CuPc-COF.

Furthermore, the nucleation mechanism of Zn^{2+} was investigated by chronoamperometry (Figure S20, Supporting Information). The current time curve can sensitively reflect the nucleation process of Zn. For the bare Zn electrode, the current density decreased after 30 s under 200 mV, indicating the two-dimensional diffusion behavior of Zn^{2+} on the surface and rough Zn deposition. However, under the same potential, the current density of the COF@Zn electrode decreased rapidly and remained within 5s, revealing a stable three-dimensional Zn^{2+} diffusion on the COF@Zn surface. This points out that the ketonic carbonyl of the COF framework coordinates with Zn^{2+}, leading to the additional extra energy consumption of the movement of Zn^{2+} in the horizontal direction and effectively restraining the diffusion of Zn^{2+},[24] which also matched with the theoretical calculation about migration barriers. In contrast, the Cu active sites of the COF layer serve as heterogeneous seeds for uniform Zn nucleation and when combined with the ion sieving channels provide continual regulation for dendrite-free Zn deposition. Thus, the COF@Zn electrode owing to the protective COF layer remains a uniform and compact surface without obvious dendrites. It strongly demonstrated that the nanoscale cavities and the adjusted charge distribution on the COF layer can induce even Zn plating toward the electrode, thereby effectively restraining the Zn dendrite formation and growth.

Based on the above discussion, the Zn deposition process on two different electrodes can be summarized in Figure 3n. Because of the rough surface of the bare Zn foil, Zn^{2+} is preferably nucleated at the protrusion to form dendritic Zn. Conversely, the unique porous structures of the COF layer provided a short and straightforward Zn^{2+} diffusion pathway, thus endowing the facile access of Zn^{2+} toward the ketonic carbonyl and Cu active sites. Meanwhile, the Cu-based COF@Zn layer presented an inert nature for HER, effectively alleviating hydrogen evolution and anode corrosion in aqueous electrolytes. Thus, the COF@Zn anode enabled strong Zn^{2+} modulation behavior from the initial nucleation to the subsequent mass-transfer processes. This may lead to subsequent uniform galvanization in the COF cavity with a smooth, dendrite-free zinc plating morphology. The unique porous character, robust structure, and low volumetric expansion during zincification/dezincification facilitate the active sites of COF@Zn anode highly accessible to achieve rapid and reversible Zn deposition/stripping. Additionally, CuPc-COF served as the inhibitor to eliminate the hydrogen evolution side reactions, could realize the excellent cycling lifespan. Equally importantly, the robust structure, electrolyte insolubility, and low volumetric expansion during zincification/dezincification also ensure a reliable electrode for stable Zn^{2+} storage.

To explore the feasibility of as-prepared anode for practical application, the electrochemical performance of Zn/NHVO full cell with COF@Zn anode was evaluated as schematically shown in **Figure 4**a. The cyclic voltammetry (CV) curves of COF@Zn/NHVO and Zn/NHVO cells presented similar redox peaks, indicating the identical Zn^{2+} deintercalation and intercalation processes (Figure 4b). Compared to a Zn/NHVO cell, the redox peaks of COF@Zn/NHVO cell delivered a smaller potential shift, exhibiting the accelerated ion transmission kinetics to regulate the Zn^{2+} migration behavior. Nyquist plots of these two full cells using different anodes are also provided (Figure 4c). The smaller charge-transfer resistance (R_{ct}) of COF@Zn/NHVO cell (69 Ω) than that of the bare Zn (106 Ω) implied the accelerated Zn^{2+} migration process. Additionally, the charge/discharge curves under current density of 0.2 A•g^{-1} (Figure S21a, Supporting Information) further confirmed the significantly improved interface kinetics in the COF@Zn/NHVO cell. Accordingly, their rate performance under current densities ranging from 0.5 to 2.0 A•g^{-1} was compared (Figure 4d). Specifically, the COF@Zn/NHVO cell delivered enhanced rate capacities, where the specific capacities at 0.5, 0.8, 1, and 2.0 A•g^{-1} were 279, 241, 201, and 143 mAh•g^{-1}, respectively. The corresponding charge/discharge curves are shown in Figure S21b (Supporting Information). Finally, the long-term stability of a full cell under a high current density of 1 A•g^{-1} was performed (Figure 4e).

© 2025 The Author(s). Advanced Materials published by Wiley-VCH GmbH

15214095, 2025, 33, Downloaded from https://advanced.onlinelibrary.wiley.com/doi/10.1002/adma.202503086 by HONG KONG POLYTECHNIC UNIVERSITY HU NG HOM, Wiley Online Library on [28/09/2025]. See the Terms and Conditions (https://onlinelibrary.wiley.com/terms-and-conditions) on Wiley Online Library for rules of use; OA articles are governed by the applicable Creative Commons License

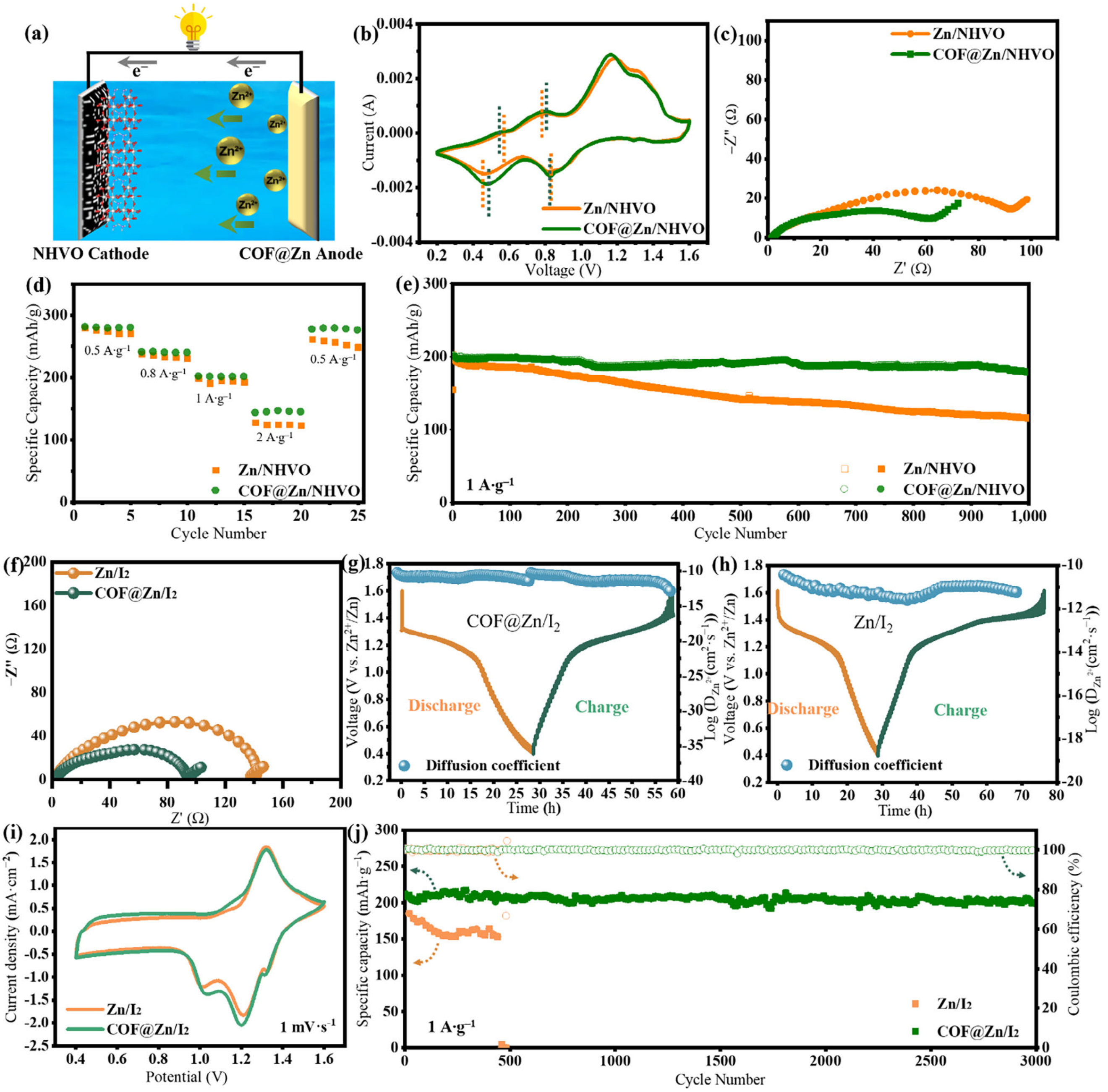

Figure 4. a) Schematic illustration of the COF@Zn/NHVO full cell. b) CV curves, c) Nyquist plots, d) rate performance and e) cycling performance of Zn/NHVO and COF@Zn/NHVO full cells. f) The Nyquist plots of Zn/I_2 and COF@Zn/I_2 full cells. The Galvanostatic Intermittent Titration Technique (GITT) curve and ionic diffusion coefficient of g) COF@Zn/I_2 and h) Zn/I_2 full cells. i) The CV curves of the Zn/I_2 and COF@Zn/I_2 full cells with the scan rate of 1 mV s^{-1}. j) The cycling performance of the Zn/I_2 and COF@Zn/I_2 full cells.

The Zn/NHVO cell delivered an initial capacity of 201 mAh•g^{-1}, with a superior capacity retention ratio of 89.1% after 1000 cycles. Overall, the above results strongly confirm the practical applicability of the COF@Zn anode in COF@Zn/NHVO full cells. The robust ion-modulating structure of the COF layer significantly enhances the cycle life and capacity retention of the battery, outperforming other conventional modified anodes in the previous literature papers, as illustrated in Table S1 (Supporting Information).[25]

The Zn/I_2 full cell was further constructed using the COF@Zn anode in conjunction with the iodine cathode for electrochemical testing. As displayed in Figure 4f, the R_{ct} value decreased from 142 to 93 Ω after the application of the COF layer, indicating the enhanced charge transfer kinetics. Besides, the COF@Zn/I_2 cell presented larger Zn^{2+} diffusion coefficient (1.29×10^{-11} $cm^2 \cdot s^{-1}$ vs 8.44×10^{-12} cm^2 s^{-1}) than the Zn/I_2 cell arising from improved reaction kinetics for the COF@Zn anode (Figure 4g,h).[26] The CV profiles of the COF@Zn/I_2 cell also delivered broader

© 2025 The Author(s). Advanced Materials published by Wiley-VCH GmbH

15214095, 2025, 33, Downloaded from https://advanced.onlinelibrary.wiley.com/doi/10.1002/adma.202503086 by HONG KONG POLYTECHNIC UNIVERSITY HU NG HOM, Wiley Online Library on [28/09/2025]. See the Terms and Conditions (https://onlinelibrary.wiley.com/terms-and-conditions) on Wiley Online Library for rules of use; OA articles are governed by the applicable Creative Commons License

15214095, 2025, 33, Downloaded from https://advanced.onlinelibrary.wiley.com/doi/10.1002/adma.202503086 by HONG KONG POLYTECHNIC UNIVERSITY HU NG HOM, Wiley Online Library on [28/09/2025]. See the Terms and Conditions (https://onlinelibrary.wiley.com/terms-and-conditions) on Wiley Online Library for rules of use; OA articles are governed by the applicable Creative Commons License

reversible redox peaks than those of the Zn/I$_2$ cell, indicating higher electrochemical activity due to the increased active sites for redox reactions and ion intercalation/deintercalation processes (Figure 4i).[27] As shown in Figure S22 (Supporting Information), the Zn/I$_2$ cell with the COF@Zn anode demonstrated an initial discharge capacity of 212.3 mAh·g^{-1} at 1 A·g^{-1}, surpassing that of the bare Zn anode (198.9 mAh·g^{-1}). The charge–discharge curve of COF@Zn anode showed a reduced polarization gap compared to the bare Zn anode, indicating faster reaction kinetics. More impressively, compared with the severe capacity decay of the bare Zn anode within 500 cycles, the COF@Zn anode achieved a capacity retention of 92.9% after 3000 cycles, demonstrating enhanced reversibility and cycle stability (Figure 4j).

3. Conclusion

In conclusion, we proposed a highly conjugated robust CuPc-COF with customized Zn^{2+} migration channels and HER-inert metal center (Cu^{2+}) for the Zn anode protective layer. Benefiting from the precisely designed structures, this CuPc-COF effectively promotes the de-solvation of hydrated Zn^{2+}, accelerates the ion transfer kinetics, and regulates the Zn^{2+} flux, simultaneously inhibiting the zinc dendrites and hydrogen evolution side reactions. As a result, the COF@Zn electrode delivers excellent electrochemical behaviors including outstanding reversible capacity (over 99% in average Coulombic efficiency), high-rate capability (5 mA•cm^{-2}), superior cycling stability of 2500 h for the symmetric cell at 1 mA•cm^{-2}, accelerated the ion transmission kinetics, and preeminent cyclability (1000 cycles at 1 A•g^{-1} and 3000 cycles at 1 A•g^{-1}) of full cells paired with NHVO cathode and I$_2$ cathode, respectively. In summary, the rational molecular design of CuPc-COF protective layer provides a promising modulation strategy for directional Zn deposition and opens a new avenue of metallated COF materials for dendrite-free Zn anodes in long-term AZIBs.

Supporting Information

Supporting Information is available from the Wiley Online Library or from the author.

Acknowledgements

W.Y.W. is grateful to the financial support from the Hong Kong Research Grants Council (PolyU 15307321), the RGC Senior Research Fellowship Scheme (SRFS2021-5S01), Research Institute for Smart Energy (CDAQ), Research Centre for Nanoscience and Nanotechnology (CE2H) and Miss Clarea Au for the Endowed Professorship in Energy (847S). Y.W. is thankful for support from the National Natural Science Foundation of China (22309156). The authors also acknowledge the University Research Facility in Life Sciences (ULS) for help in the matrix-assisted laser desorption ionization time-of-flight mass spectrometry tests.

Conflict of Interest

The authors declare no conflict of interest.

Data Availability Statement

The data that support the findings of this study are available from the corresponding author upon reasonable request.

Keywords

2D porous materials, artificial interlayer, covalent organic frameworks, phthalocyanine, zinc-ion batteries

Received: February 14, 2025
Revised: May 7, 2025
Published online: June 5, 2025

[1] a) H. H. Heenen, H. Shin, G. Kastlunger, S. Overa, J. A. Gauthier, F. Jiao, K. Chan, *Energy Environ. Sci.* **2022**, *15*, 3978; b) H. Dong, J. Li, J. Guo, F. Lai, F. Zhao, Y. Jiao, D. J. L. Brett, T. Liu, G. He, I. P. Parkin, *Adv. Mater.* **2021**, *33*, 2007548.

[2] a) G. Fang, J. Zhou, A. Pan, S. Liang, *ACS Energy Lett.* **2018**, *3*, 2480; b) Y. Shi, Y. Chen, L. Shi, K. Wang, B. Wang, L. Li, Y. Ma, Y. Li, Z. Sun, W. Ali, S. Ding, *Small* **2020**, *16*, 2000730; c) P. Xiao, H. Li, J. Fu, C. Zeng, Y. Zhao, T. Zhai, H. Li, *Energy Environ. Sci.* **2022**, *15*, 1638.

[3] a) H. Jia, K. Liu, Y. Lam, B. Tawiah, J. Xin, W. Nie, S. Jiang, *Adv. Fiber Mater.* **2022**, *5*, 36; b) Q. Li, D. Wang, B. Yan, Y. Zhao, J. Fan, C. Zhi, *Angew. Chem., Int. Ed.* **2022**, *61*, 202202780; c) Q. Yang, Q. Li, Z. Liu, D. Wang, Y. Guo, X. Li, Y. Tang, H. Li, B. Dong, C. Zhi, *Adv. Mater.* **2020**, *32*, 2001854.

[4] a) Z. C. Qi, T. Xiong, T. Chen, C. Yu, M. C. Zhang, Y. Yang, Z. J. Deng, H. Xiao, W. S. V. Lee, J. M. Xue, *ACS Appl. Mater. Interfaces* **2021**, *13*, 28129; b) L. Zhang, B. Zhang, T. Zhang, T. Li, T. F. Shi, W. Li, T. Shen, X. X. Huang, J. J. Xu, X. G. Zhang, Z. Y. Wang, Y. L. Hou, *Adv. Funct. Mater.* **2021**, *31*, 2100186; c) Y. Guo, C. Liu, L. Xu, K. X. Huang, H. Wu, W. L. Cai, Y. Zhang, *Energy Mater.* **2022**, *2*, 200032.

[5] a) L. Yuan, J. Hao, C.-C. Kao, C. Wu, H.-K. Liu, S.-X. Dou, S.-Z. Qiao, *Energy Environ. Sci.* **2021**, *14*, 5669; b) F. Wu, Y. Chen, Y. Chen, R. Yin, Y. Feng, D. Zheng, X. Xu, W. Shi, W. Liu, X. Cao, *Small* **2022**, *18*, 2202363; c) L. Zhou, F. Yang, S. Zeng, X. Gao, X. Liu, X. Cao, P. Yu, X. Lu, *Adv. Funct. Mater.* **2022**, *32*, 2110829; d) H. Jia, Q. Ming, C. Lan, H. Liu, M. Dirican, S. Fu, X. Zhang, *Adv. Sci.* **2021**, *2103952*, 1; e) L. Ma, M. A. Schroeder, O. Borodin, T. P. Pollard, M. S. Ding, C. Wang, K. Xu, *Nat. Energy* **2020**, *5*, 743; f) X. Zeng, J. Mao, J. Hao, J. Liu, S. Liu, Z. Wang, Y. Wang, S. Zhang, T. Zheng, J. Liu, P. Rao, Z. Guo, *Adv. Mater.* **2021**, *33*, 2007416.

[6] a) L. T. Hieu, S. So, I. T. Kim, J. Hur, *Chem. Eng. J.* **2021**, *411*, 128584; b) Z. Zhao, J. Zhao, Z. Hu, J. Li, J. Li, Y. Zhang, C. Wang, G. Cui, *Energy Environ. Sci.* **2019**, *12*, 1938.

[7] a) J. Zhou, M. Xie, F. Wu, Y. Mei, Y. Hao, R. Huang, G. Wei, A. Liu, L. Li, R. Chen, *Adv. Mater.* **2021**, *33*, 2101649; b) X. Zhang, Q. Ruan, L. Liu, D. Li, Y. Xu, Y. Wang, J. Liu, C. Huang, F. Xiong, B. Wang, P. K. Chu, *J. Electroanal. Chem.* **2023**, *936*, 117357.

[8] a) K. Zhao, C. Wang, Y. Yu, M. Yan, Q. Wei, P. He, Y. Dong, Z. Zhang, X. Wang, L. Mai, *Adv. Mater. Interfaces* **2018**, *5*, 1800848; b) P. Liang, J. Yi, X. Liu, K. Wu, Z. Wang, J. Cui, Y. Liu, Y. Wang, Y. Xia, J. Zhang, *Adv. Funct. Mater.* **2020**, *30*, 1908528.

[9] a) L. Lei, B. Zhao, X. Pei, L. Gao, Y. Wu, X. Xu, P. Wang, S. Wu, S. Yuan, *ACS Appl. Mater. Interfaces* **2024**, *16*, 485; b) P. Li, J. Ren, C. Li, J. Li, K. Zhang, T. Wu, B. Li, L. Wang, *Chem. Eng. J.* **2023**, *451*, 138769.

[10] a) Y. Wang, N. Li, H. Liu, H. Sun, Z. Wang, L. Zhai, K. Chen, L. Mi, Z. Fang, Y. Huang, *J. Mater. Chem. A* **2024**, *12*, 7799; b) L. Liang, L. Su, X. Zhang, Y. Wang, W. Ren, X. Gao, L. Zheng, F. Lu, *Chem. Eng. J.* **2024**, *485*, 149813; c) B. Li, P. Ruan, X. Xu, Z. He, X. Zhu, L. Pan, Z. Peng, Y. Liu, P. Zhou, B. Lu, L. Dai, J. Zhou, *Nano-Micro Lett.* **2024**,

© 2025 The Author(s). Advanced Materials published by Wiley-VCH GmbH

16, 76; d) P. Liu, J. Guo, S. Gao, P. Zeng, Q. Zhang, T. Wang, D. Wu, K. Liu, *J. Colloid Interface Sci.* **2023**, *648*, 520; e) L. Yang, Q. Ma, Y. Yin, D. Luo, Y. Shen, H. Dou, N. Zhu, R. Feng, Y. Kong, A. Yu, B. Cheng, X. Wang, Z. Chen, *Nano Energy* **2023**, *117*, 108799; f) C. Guo, X. Huang, J. Huang, X. Tian, Y. Chen, W. Feng, J. Zhou, Q. Li, Y. Chen, S. L. Li, Y. Q. Lan, *Angew. Chem., Int. Ed.* **2024**, *63*, 202403918; g) C. Guo, J. Zhou, Y. Chen, H. Zhuang, Q. Li, J. Li, X. Tian, Y. Zhang, X. Yao, Y. Chen, S.-L. Li, Y.-Q. Lan, *Angew. Chem., Int. Ed.* **2022**, *61*, 202210871; h) J. H. Park, M.-J. Kwak, C. Hwang, K.-N. Kang, N. Liu, J.-H. Jang, B. A. Grzybowski, *Adv. Mater.* **2021**, *33*, 2101726; i) X. Wang, P. Shao, S. Bai, R. Yang, X. Jin, C. Zhi, B. Wang, *Batteries Supercaps.* **2023**, *6*, 202300099; j) Z. Zhao, R. Wang, C. Peng, W. Chen, T. Wu, B. Hu, W. Weng, Y. Yao, J. Zeng, Z. Chen, P. Liu, Y. Liu, G. Li, J. Guo, H. Lu, Z. Guo, *Nat. Commun.* **2021**, *12*, 6606; k) D. Zhu, G. Xu, M. Barnes, Y. Li, C.-P. Tseng, Z. Zhang, J.-J. Zhang, Y. Zhu, S. Khalil, M. M. Rahman, R. Verduzco, P. M. Ajayan, *Adv. Funct. Mater.* **2021**, *31*, 2100505; l) J. Zhao, Y. Ying, G. Wang, K. Hu, Y. D. Yuan, H. Ye, Z. Liu, J. Y. Lee, D. Zhao, *Energy Storage Mater.* **2022**, *48*, 82.

[11] a) T. Wang, L. Guo, Z. Jiang, S. Chen, S. Xu, Y. Zhang, J. Zhang, R. Li, T. Peng, *Adv. Funct. Mater.* **2021**, *31*, 2107290; b) M. Fang, L. Xu, H. Zhang, Y. Zhu, W. Y. Wong, *J. Am. Chem. Soc.* **2022**, *144*, 15143.

[12] a) T. Ujiro, S. Satoh, R. W. Staehle, W. H. Smyrl, *Corros. Sci.* **2001**, *43*, 2185; b) G. Gao, S. Bottle, A. Du, *Catal. Sci. Technol.* **2018**, *8*, 996.

[13] a) A. T. Chidembo, K. I. Ozoemena, B. O. Agboola, V. Gupta, G. G. Wildgoose, R. G. Compton, *Energy Environ. Sci.* **2010**, *3*, 228; b) L. Mei, X. Cui, Q. Duan, Y. H. Li, X. L. Lv, H. G. Wang, *Int. J. Hydrogen Energy* **2020**, *45*, 22950; c) T. Hosokawa, M. Tsuji, K. Tsuchida, K. Iwase, T. Harada, S. Nakanishi, K. Kamiya, *J. Mater. Chem. A* **2021**, *9*, 11073.

[14] S. Tao, C. Zhang, J. Zhang, Y. Jiao, M. Li, W. Lin, L. Ran, B. Clement, M. Lyu, I. Gentle, L. Wang, R. Knibbe, *Chem. Eng. J.* **2022**, *446*, 136607.

[15] B. Liu, Y. Zhang, Z. Wang, C. Ai, S. Liu, P. Liu, Y. Zhong, S. Lin, S. Deng, Q. Liu, G. Pan, X. Wang, X. Xia, J. Tu, *Adv. Mater.* **2020**, *32*, 2003657.

[16] H. Jia, M. Qiu, C. Tang, H. Liu, J. Xu, B. Tawiah, S.-x. Jiang, X. Zhang, *Adv. Fiber Mater.* **2022**, *4*, 1500.

[17] H. Sun, Y. Huyan, N. Li, D. Lei, H. Liu, W. Hua, C. Wei, F. Kang, J.-G. Wang, *Nano Lett.* **2023**, *23*, 1726.

[18] A. Xie, X. You, R. Zhang, J. Miao, L. Cheng, X. Tai, Z. Qin, Y. Tang, X. Yang, Y. Chen, P. Wan, *J. Colloid Interface Sci.* **2023**, *638*, 629.

[19] F. Zhang, T. Liao, C. Liu, H. Peng, W. Luo, H. Yang, C. Yan, Z. Sun, *Nano Energy* **2022**, *103*, 107830.

[20] a) S. Zheng, D. Shi, D. Yan, Q. Wang, T. Sun, T. Ma, L. Li, D. He, Z. Tao, J. Chen, *Angew. Chem., Int. Ed.* **2022**, *61*, 202117511; b) R. J. Shi, L. J. Liu, Y. Lu, C. C. Wang, Y. X. Li, L. Li, Z. H. Yan, J. Chen, *Nat. Commun.* **2020**, *11*, 178.

[21] a) X. L. Chen, M. Xie, Z. L. Zheng, X. Luo, H. Jin, Y. F. Chen, G. Z. Yang, D. S. Bin, D. Li, *J. Am. Chem. Soc.* **2023**, *145*, 5105; b) S. Zhang, Y. L. Zhu, S. Ren, C. Li, X. B. Chen, Z. Li, Y. Han, Z. Shi, S. Feng, *J. Am. Chem. Soc.* **2023**, *145*, 17309.

[22] H. J. Yang, Y. Qiao, Z. Chang, H. Deng, P. He, H. S. Zhou, *Adv. Mater.* **2020**, *32*, 2004240.

[23] S. Li, Y. Liu, X. Zhao, Q. Shen, W. Zhao, Q. Tan, N. Zhang, P. Li, L. Jiao, X. Qu, *Adv. Mater.* **2021**, *33*, 2007480.

[24] Y. Mao, Z. Li, Y. Li, D. Cao, G. Wang, K. Zhu, G. Chen, *Chem. Eng. J.* **2023**, *461*, 141707.

[25] a) Y. F. Huang, Z. W. Chang, W. B. Liu, W. T. Huang, L. B. Dong, F. Y. Kang, C. J. Xu, *Chem. Eng. J.* **2022**, *431*, 133902; b) R. W. Meng, H. Li, Z. Y. Lu, C. Zhang, Z. X. Wang, Y. X. Liu, W. C. Wang, G. W. Ling, F. Y. Kang, Q. H. Yang, *Adv. Mater.* **2022**, *34*, 2200677; c) W. T. Zhou, Z. T. Chen, S. S. Zhao, S. M. Chen, *Adv. Funct. Mater.* **2024**, *34*, 2409520; d) H. S. Lin, S. J. Cai, L. Y. Li, Z. Y. Ma, X. Y. Wang, S. Q. Liang, G. Z. Fang, M. J. Xiao, Z. G. Luo, *Small Methods* **2025**, *9*, 2401096; e) J. M. Jiang, Z. H. Pan, J. R. Yuan, J. Shan, C. L. Chen, S. P. Li, Y. X. Chen, Q. C. Zhuang, Z. C. Ju, H. Dou, X. G. Zhang, J. Wang, J. H. Wang, *Chem. Eng. J.* **2023**, *452*, 139335; f) C. B. Yuan, C. Liu, X. T. Li, Y. H. Zhi, X. W. Zhan, S. Gao, *ACS Appl. Mater. Interfaces* **2023**, *6*, 1897.

[26] Q. Liu, Z. L. Yu, K. Fan, H. T. Huang, B. Zhang, *ACS Nano* **2024**, *18*, 22484.

[27] Z. L. Li, W. W. Cao, T. Hu, Y. C. Hu, R. Zhang, H. L. Cui, F. N. Mo, C. Z. Liu, C. Y. Zhi, G. J. Liang, *Angew. Chem., Int. Ed.* **2024**, *63*, 202317652.

© 2025 The Author(s). Advanced Materials published by Wiley-VCH GmbH

15214095, 2025, 33, Downloaded from https://advanced.onlinelibrary.wiley.com/doi/10.1002/adma.202503086 by HONG KONG POLYTECHNIC UNIVERSITY HU NG HOM, Wiley Online Library on [28/09/2025]. See the Terms and Conditions (https://onlinelibrary.wiley.com/terms-and-conditions) on Wiley Online Library for rules of use; OA articles are governed by the applicable Creative Commons License